A Case Study of the Radiative Forcing of Persistent Contrails Evolving into Contrail-Induced Cirrus

James M. Haywood[1], Richard P. Allan[2], Jorge Bornemann[1], Piers Forster[3], Peter N. Francis[1], Sean Milton[1], Gaby Rädel[4], Alexandru Rap[3], Keith P. Shine[4] and Robert Thorpe[1].

[1]Met Office, Exeter, UK

[2]ESSC, University of Reading, UK.

[3]Dept of Environmental Science, University of Leeds, UK.

[4]Dept of Meteorology, University of Reading, UK.

Abstract

The radiative forcing due to a distinct pattern of persistent contrails that form into contrail-induced cirrus near and over the UK is investigated in detail for a single case study during March 2009. The development of the cirrus is tracked using a number of high-resolution polar orbiting and lower resolution geostationary satellite instruments. The cirrus is found to persist for a period of around 18 hours and, at its peak, covers over 50,000km^2. The shortwave (SW) and longwave (LW) radiative forcing of the contrail-induced cirrus is estimated using a combination of geostationary satellite instruments, numerical weather prediction models, and surface observation sites. As expected, the net radiative effect is a relatively small residual of the much stronger but opposing SW and LW effects, locally totalling around 10Wm^{-2} during daylight hours and 30Wm^{-2} during night-time. A simple estimate indicates that this single localised event may have generated a global-mean radiative forcing which is around 7% of recent estimates of the persistent contrail radiative forcing due to the entire global aircraft fleet on a diurnally-averaged basis. A single aircraft operating in conditions favourable for persistent contrail formation appears to exert a contrail-induced radiative forcing

some 5000 times greater (in Wm^{-2}/km) than recent estimates of the average persistent-contrail radiative forcing from the entire civil aviation fleet. This study emphasizes the need to establish whether similar events are common or highly unusual for a confident assessment of the total climate effect of aviation to be made.

1. Introduction

The rapid growth and the forecast future expansion of the aviation industry mean that the potential climatic effects have received considerable attention over the past decade (e.g. *IPCC*, 1999; *Sausen et al*, 2005*; Lee et al.* 2009). The civil aviation industry currently emits around 2-3% of all carbon dioxide emissions on a global basis, but the total impact upon the Earth radiation budget is thought to be higher primarily because of the radiative impact of persistent condensation trails (contrails) and aviation-induced cirrus. Aviation-induced cirrus can occur through two different pathways: via contrails spreading out, and by injection of aerosols into the upper troposphere to provide ice-nuclei that may subsequently form cirrus clouds (*Lee et al*, 2009). Our study is restricted to the first of these, and we therefore refer to contrail-induced cirrus throughout this work. Contrails may form when emissions of hot, warm engine exhaust in the upper troposphere mix with the cool moist ambient atmosphere. Under certain atmospheric conditions (super-saturated with respect to ice), contrails can persist for several hours. If the atmospheric conditions are favourable for ice crystal growth these persistent contrails may grow and spread out to form contrail-induced cirrus clouds (e.g. *Fahey et al*, 1999). Persistent contrails and contrail-induced cirrus exert a radiative forcing in both the SW solar spectrum and LW terrestrial spectrum (e.g. *Stuber et al.*, 2006; *Kärcher and Spichtinger*, 2009). They reflect incident sunlight back to space thereby brightening the planet and leading to a negative SW radiative forcing that is associated with a cooling. They also trap LW radiation within the Earth atmosphere system leading to a positive LW radiative forcing that is associated with a warming. The net radiative effect of persistent contrails and contrail-induced cirrus is the sum of the negative SW radiative forcing and positive LW radiative forcing, resulting in a net

53 forcing that is believed to be positive but rather small in magnitude (e.g. *Myhre and Stordal*, 2001,
54 *Stuber et al*, 2006, *Rädel and Shine,* 2008).
55
56 The earliest comprehensive estimate of the impact of aviation emissions for aircraft operations in
57 1992 (*Prather et al*, 1999; *IPCC*, 1999) suggested a radiative forcing of 20mWm^{-2} for the formation
58 of persistent contrails with considerable uncertainty. The estimate of the radiative forcing from
59 contrail-induced cirrus was thought to be so uncertain that it could not even be quantified. The
60 relative importance of persistent contrails and contrail-induced cirrus has been estimated in more
61 recent studies at 10mWm^{-2} by *Sausen et al.* (2005) and 30mWm^{-2} (range 10 to 80mWm^{-2}) by *Stordal*
62 *et al* (2005). The assessment of persistent contrails was adopted by *Forster et al* (2007) and *IPCC*
63 (2007) who assigned a 90% confidence interval of 6mWm^{-2} to 30mWm^{-2}. *Forster et al.* (2007) also
64 point out the inherent ambiguity in trying to determine and separate aviation-induced cloudiness
65 from persistent line shaped contrails: the line-shaped contrails typically shear and spread and lose
66 their characteristic shape while evolving into contrail-induced cirrus (e.g. *Minnis et al.*, 1998). Thus
67 estimates of the ratio of the RF from contrail-induced cirrus to persistent contrails are highly
68 uncertain and range from about 1 to 8 (e.g. *Lee et al.* 2009). These estimates of the radiative forcing
69 of contrail-induced cirrus typically are derived from satellite retrievals by considering the spatial
70 correlation of the radiances in water vapour, infra-red, and/or solar channels with aviation traffic
71 routes and by applying suitable threshold criteria (e.g. *Minnis et al.*, 1998; 2004; *Mannstein and*
72 *Schumann*, 2005) but the difficulties in distinguishing contrail-induced cirrus from natural cirrus are
73 severe (*Mannstein and Schumann* 2007).
74
75 The uncertainty in estimates of the radiative forcing of persistent linear contrails and the evolution
76 into contrail-induced cirrus means that observational case studies are necessary to better understand
77 their physical and radiative properties. *Minnis et al* (1998) used geostationary satellite instruments to
78 track distinctly-shaped contrails evolving into cirrus in three separate events during April-May 1996

and detailed the microphysical evolution of the cirrus particles together with the cirrus optical depth cloud top temperature and area extent. Essentially, we perform a similar study, but use polar orbiting satellite data that is available at higher frequency nowadays to track the evolution of a characteristic contrail shape as it evolved into cirrus. We extend the approach of *Minnis et al.* (1998) by utilising surface and satellite measurements in conjunction with operational numerical weather prediction (NWP) models to isolate both the SW and LW RF of the contrail-induced cirrus. Unlike other studies (e.g. *Rap et al.*, 2009), our methodology does not rely on explicit modelling of the persistent contrails/contrail-induced cirrus themselves. The radiative forcing is deduced by subtracting the irradiances from satellite observations of persistent contrails/contrail induced cirrus from the irradiances derived from the NWP model which does not include contrails.

A distinct coil-shaped contrail/cirrus (hereafter CCC) that is thought to have originated from manoeuvres performed by an Airborne Warning and Control System (AWACS) aircraft was observed in satellite imagery during March 2009 (Figure 1). Figure 1a shows that the CCC is difficult to detect in visible imagery (image shown in the High Resolution Visible, HRV, from the SEVIRI instrument) owing to the presence of extensive stratocumulus cloud at lower levels. Indeed the shadow of the contrail on the lower stratocumulus clouds, which causes a reduction in reflectance, is more readily detectable than any increase in reflectance. Figure 1b shows that the CCC is however very readily discernable in the infra-red wavelengths because of the large difference in the emission temperature between the CCC and the low level stratocumulus. Both images show that while the CCC is by far the most distinguishable contrail occurring over the North Sea, several other contrails are also visible off the coast of Scotland and England and encroach over S.E. England.

In this study we analyse the meteorological conditions which are shown to favour persistent contrail formation between approximately 25,000-35,000ft (7.5 to 10.5km) (section 2). Polar orbiting

satellite instruments that detect cloud at infra-red (10.8μm) wavelengths are used to record the evolution of the CCC over a ten hour period and atmospheric dispersion model is used to verify the position of the coil-shaped contrail as it shears and spreads (section 3). The study also uses independent measurements from the geostationary Meteosat-9 satellite Spinning Enhanced Visible and InfraRed Imager (SEVIRI) instrument to track the CCC and other persistent contrails as they advect and evolve. Although the evolution of ice crystal effective radius cirrus optical depth are hampered by the presence of low-level stratocumulus and the advection over variable land surfaces, retrievals are possible over ocean surfaces free from low level cloud (section 4). The advection of the contrail/cirrus over land means that instrumented meteorological observation sites may also be used to determine the SW radiative forcing at the surface (section 5). The SW and the LW top of the atmosphere radiative forcings are estimated by comparing the SW and LW irradiances derived from the Met Office high resolution (4km) UK4 operational NWP model (section 6.). A discussion and conclusion and then provided (section 7).

2. The prevailing meteorological conditions.

The synoptic surface analysis chart for 12:00 (all times refer to UTC) on 20 March 2009 is shown in Figure 2. A large anti-cyclone is centred on the UK with a central surface pressure of around 1034-1035hPa. The UK is in a stable warm sector with a weak frontal systems approaching only very slowly from the west. The small pressure gradients mean that wind is slack across the UK. Figure 3 shows the tephigrams derived from radiosonde ascents from Met Office sites for 12:00 for Nottingham (53.00^{o}N, 1.25^{o}W), Albermarle (55.01^{o}N, 1.52^{o}W), and Ekofisk (56.53^{o}N, 3.21^{o}E) (see geographical positions marked on Figure 1). *Rädel and Shine* [2007] have shown that provided corrections are made to the relative humidity derived from these sondes, they can be used quite reliably to infer conditions necessary for the formation of persistent contrails. All three of the tephigrams show a strong subsidence temperature inversion indicating highly stable atmospheric conditions to around 600hPa. At low levels the atmosphere is dry with water vapour mass mixing

131 ratios lower than 0.2-0.4gkg^{-1} evident in the Nottingham and Ekofisk ascents. The lack of moisture
132 in the atmospheric column is reflected by the low total precipitable water values of 5.2mm, 8.5mm,
133 and 6.7mm for the Nottingham, Albermarle, and Ekofisk ascents respectively. At upper levels, the
134 Ekofisk sounding shows a similar temperature profile to the other two radiosonde ascents, but the
135 water vapour mass mixing ratio is significantly higher between 250-500hPa indicating a moister
136 upper troposphere. The relative humidity with respect to ice calculated from the profiles making the
137 corrections to relative humidity recommended by *Rädel and Shine* [2007] based on *Vömel et al*
138 [2007] is shown in Figure 3b. At upper levels, the relative humidity only very slightly exceeds 100%
139 for Nottingham, but exceeds 100% for Albermarle above about 275hPa. For the Ekofisk ascent a
140 much greater altitude range (200-400hPa) is subject to ice supersaturation conditions meaning that
141 persistent contrail formation and growth may therefore be confidently expected near the Ekofisk oil
142 platform provided that the ambient temperature is below the minimum temperature for contrail
143 formation: the Ekofisk tephigrams reveals a temperature at 300hPa of around -50C which is
144 sufficient for contrail initiation. Thus one might expect contrails to be initiated and spread around the
145 Ekofisk region of the N Sea. This is consistent with visual inspection of the contrails shown in
146 Figure 1.
147
148 Inspection of fields of the relative humidity with respect to ice from the operational UK4 model
149 reveals that, although the relative humidity with respect to ice frequently approaches 100%, no areas
150 of super-saturation are found over the North Sea between pressure levels of 300-350hPa over the
151 period 12:00 on the 20 March 2009 to 06:00 on the 21 March 2009. In common with many of the
152 current Met Office Numerical Weather Prediction models (e.g. *Newman et al*, 2008) and the climate
153 model (*Rap et al*., submitted manuscript), this deficiency in model performance appears to be linked
154 to too dry a modelled upper troposphere. Not all operational NWP models exhibit this deficiency.
155 Figure 4 shows the relative humidity with respect to ice determined from a 12 hour forecast of
156 ECMWF operational model. The forecast relative humidity over the North Sea at 12:00 is seen to

exceed 100% between levels of 25,000-35,000ft (9.8-11.2km), with peak values exceeding 130% above 32,500ft (~11km).

Further efforts are obviously needed to improve the Met Office suite of models in terms of their upper tropospheric moisture, particularly if the Met Office is to improve its contrail forecasting capability from the model. However, here we turn this deficit to our advantage: because the model does not predict any significant ice super-saturation and hence no upper level cirrus, the difference between the modelled and observed radiative fluxes at the top of the atmosphere are essentially equivalent to the radiative forcing of the contrails/cirrus. This methodology assumes that the radiative effect of the moisture deficit is second-order compared to the radiative effect of the contrails, which radiative transfer calculations show to be a reasonable assumption. Such an approach has previously been used for determining the radiative effects of mineral dust over the Sahara desert (*Haywood et al.*, 2005). One particularly significant advantage of this approach is that it does not rely to any degree on accurate modelling of the detailed microphysics and spatial distribution of the contrails/cirrus: only radiative transfer in the absence of contrails/cirrus needs to be performed. This methodology will be considered in more detail in section 6.

3. Evolution of the contrails into cirrus.

As shown in Figure 1, the CCC is most readily distinguished from the low-level stratocumulus cloud using infra-red (10.8μm) wavelengths. Figure 5 shows the evolution of the CCC. The earliest image that shows the presence of the CCC is at 10:06 where five complete orbits are shown. By 11:30 the CCC has advected to the south but retains its characteristic shape which now contains 10 full orbits. Thus 1 orbit takes approximately 17mins. By 12:02, the CCC is becoming more difficult to identify owing to shear and diffusion smearing the characteristic shape of the CCC and by the mixing with other contrails. By 15:26 all initial resemblance to the coil shape has all but vanished and the casual observer would be forgiven for thinking that the resulting cirrus was an entirely natural feature;

183 indeed, we are unable to definitively rule out the possibility that entirely natural cirrus could have
184 formed anyway. The contrail-induced cirrus then persists over the UK until at least 19:48 and is
185 advected southwards over the Isle of Wight as shown by the final frame of Figure 5. Further imagery
186 from 03:32 on 21 March 2009 (not shown for reasons of brevity) suggests that contrail-induced
187 cirrus is still present over SW England, although this cirrus was likely generated from contrails
188 forming to the north and west of the distinctively shaped CCC.
189
190 By considering the time evolution of the CCC we can deduce that the first orbit would have been
191 started at around 08:30 and that the contrail formation from the aircraft ceased around 11:50. To
192 show beyond reasonable doubt that the CCC is still over the UK by 19:48, we initiate the Met Office
193 Numerical Atmospheric-dispersion Modelling Environment (NAME) model. NAME is a Lagrangian
194 particle model (*Ryall and Maryon*, 1998) in which emissions from pollutant sources are represented
195 by parcels released into a model atmosphere driven by the meteorological fields from the Met Office
196 global, North Atlantic Environment, or UK4 NWP models. Each parcel carries mass of one or more
197 pollutant species. The mass can change due to various physical and chemical processes during its
198 lifespan. Although originally designed as an emergency-response nuclear accident model,
199 subsequent development has greatly enhanced NAME's capabilities so that it is now used in a wide
200 range of applications (*Jones*, 2004). The NAME model was initiated using UK4 model data and
201 emission rate of particulate mass of 1g/second at an altitude of 30,000ft (9km) in a fixed circle
202 centred on 55.3^{o}N, 1^{o}E with a radius of 20km. The emission rate is entirely arbitrary, and bares no
203 resemblance to engine particulate or water vapour emissions. The size and location of the circular
204 orbit were determined by visual inspection of the satellite images. The results from the dispersion
205 model are shown in Figure 6. Figure 6a-c show that, as in the satellite images shown in Figure 5, the
206 modelled CCC is stretched in the N-S direction and by 12:02, the southernmost extent of the CCC is
207 just over the coast of the UK near the Humber estuary. Between 13:42 and 15:26 the CCC is directly
208 over the Cardington field site (see Figure 1 for the location). By 17:08 the modelled CCC lies

broadly between the Wash and the Isle of Wight and is roughly centred on the Isle of Wight by 19:48.

Throughout the first part of the period, the coherence of the CCC modelled by the NAME model and that observed by satellites is excellent which suggests that, even when the CCC becomes indistinct in the observations, the origin of the cirrus over the UK appears to be from persistent contrails. Tests with the NAME model, but with emissions now at 35,000ft (10.5km), reveal that the position of the modelled CCC is quite similar, with a similar spread and trajectory but ends in a slightly more easterly location (less than 50km difference from that shown in Figure 6h) by 19:48. Similarly, initiating the emissions at 25,000ft (7.5km) again leads to a more easterly position with the CCC being centred over London. Thus, although we cannot be certain, an emission height of 30,000ft or 9km appears to result in the best agreement between the model and satellite observations of the CCC.

This choice of emission height can be validated by independent measurements made by the Doppler lidar at the Chilbolton Observatory (for location see Figure 1). Doppler lidar attenuated backscatter is shown in Figure 7. Any cirrus signature is entirely absent from the retrievals until around 13:00, in agreement with what might be expected from the satellite observations of Figure 5. By 15:00 what we believe to be tenuous persistent contrails/contrail-induced cirrus other than those formed from the CCC are evident. The CCC is forecast to influence the retrievals from around 17:00 (see Figure 6g and 6h), and continuous cirrus is indeed detected between 7.5km and 9.5km between 17:00 and 24:00.

4. Determination of the contrail/cirrus optical depth and effective radius.

Minnis et al (1998) were able to assess the evolution of the contrail particle radii, as small contrail particles grow to become indistinguishable from natural cirrus. Our efforts are hampered by the

presence of low-level stratocumulus clouds below the contrails which make unique solutions to satellite inversion algorithms extremely challenging for operational retrievals, meaning that the particle size evolution cannot be evaluated when these low-level clouds are present. However, there are enough contrail/cirrus influenced pixels over otherwise cloud-free oceanic areas to perform a limited set of retrievals. These retrievals make use of reflectance measurements at a pair of solar wavelengths (in this case the SEVIRI channels centred at 0.8 μm and 1.6 μm), following techniques developed by *Nakajima and King* (1990), and are produced routinely at the Met Office for every 15-minutes during daylight hours.

Figure 8 shows images of the cloud optical thickness and effective radius retrieved from SEVIRI data for 14:00. The large area of liquid water stratocumulus cloud over the northern part of the North Sea is apparent, and it is this optically thick low cloud that the retrieval scheme has identified, rather than the overlying optically thin ice cloud. The areas free of low-level water cloud off the east coast of England are identified as ice cloud made up of aggregate particles having optical thicknesses generally less than around 2. Because of the thin nature of the ice cloud, the retrieval scheme encounters problems over land, and incorrectly identifies much of the thin cloud over eastern England as being water cloud. For this reason, all land pixels identified as being water cloud with an optical thickness less than 4 have been classed as ice cloud in Figure 8(a) when used in subsequent calculations and the corresponding effective radius pixels have been flagged as invalid data in Figure 8(b).

Frequency histograms of the optical thickness and effective radius are shown in Figure 9, the data here being restricted to only ice cloud retrievals over sea. Two areas are considered, the small area 52.25^{o}N to 54.6^{o}N, 0.7^{o}W to 1.4^{o}E associated with the CCC (see Figure 5 and Figure 6), and the larger area 50^{o}N to 58^{o}N, 3^{o}W to 5^{o}E to tie in with the main area of ice cloud shown in Figure 8a. Figure 9(a) shows a distribution of optical thicknesses in the CCC (dotted line) ranging between 0.4

and 1.95, with a mean value of 1.06, whereas the distribution of optical thicknesses for the remaining area (solid line) *(i.e. the difference between the large area and the small area)* shows significantly lower values, the mean value being 0.74. Equivalent effective radius distributions are shown in Figure 9(b), and these indicate that the values in the small area (dotted line) are generally lower than those in the remaining area (solid line) (mean value of 27.9 μm for the small area, mean value of 35.2 μm for the residual area).

A scatter plot of the optical thickness versus the ice effective radius is shown in Figure 9c for the CCC (red dots) and the area as a whole (black dots). As one might expect, smaller ice effective radii are associated with optically thicker cirrus of the CCC. *Minnis et al* (1998) report a change in contrail cirrus cloud effective radius from around 10μm at contrail formation to around 30μm after approximately 7.5hours. The age of the CCC is estimated from the NAME modelling work out to be around 4-5hours; our values of around 28μm are in reasonable agreement, although the rate of increase of particle size will be strongly dependent on the atmospheric conditions (*Fahey et al.*, 1999). The cause of the difference in the microphysical properties of the CCC is not investigated here, but could be due to the higher concentration of ice nuclei emitted owing to circling nature of the aircraft flight pattern or the lower estimated air-speed of the AWACS operations (estimated from the time taken to complete one complete circle of radius 20km as around 440km/hour) compared to aircraft operating at faster cruising speeds.

5. Determination of the solar SW radiative forcing from the contrails/cirrus at the surface

The radiative forcing of the contrails is determined from the Cardington field site (location shown in Figure 1) using standard Eppley solar pyranometers. Detection of the radiative effects of contrails at infra-red wavelengths is not considered here because the variation in water vapour dominates the infra-red signal. Figure 5 shows that Cardington will be affected both by the CCC and by contrails/cirrus from other sources. However, the NAME modelling of the CCC suggests that

Cardington will become directly influenced by the CCC sometime between 14:10 and 14:30. We estimate the radiative forcing in two separate ways:-

a) Determining the down-welling solar irradiance including contrails from 20 March 2009 ($SW_{\downarrow 20\ obs}$) and using simple radiative transfer modelling to determine the surface irradiance in the absence of contrails ($SW_{\downarrow 20\ model}$). The surface SW radiative forcing by contrails, ΔF_{SW}, is then given by:-

$$\Delta F_{SW\ obs\ \&\ model} = SW_{\downarrow 20\ obs} - SW_{\downarrow 20\ model} \quad (1)$$

Because the radiative transfer modelling only needs to account for Rayleigh scattering and gaseous absorption, only a very simple radiative transfer parameterisation scheme is used. Rayleigh scattering and gaseous absorption by ozone and water vapour are accounted for using the parameterisations for atmospheric transmission developed by *Lacis and Hansen* (1974) including a magnification factor to account for the curvature of the Earth and refraction of incident radiation (*Rodgers*, 1967). Ozone is estimated from the Ozone Mapping Imager (OMI) to be around 325DU, while the precipitable water vapour is from the nearby Nottingham radiosonde.

b) Determining the down-welling SW irradiance including contrails from 20 March 2009 ($SW_{\downarrow 20\ obs}$) and using observations from a cloud and contrail-free day (18 March 2009) to determine the surface irradiance from observations in the absence of contrails ($SW_{\downarrow 18\ obs}$). The surface SW radiative forcing by contrails, ΔF_{SW}, is then given by:-

$$\Delta F_{SW\ obs} = SW_{\downarrow 20\ obs} - SW_{\downarrow 18\ obs} \quad (2)$$

312 The precipitable water vapour varies from 8.3mm on 18 March 2009 at 12:00 to 5.2mm on 20 March
313 at 12:00 for the Nottingham ascent. This change in water vapour can contribute significantly to
314 differences in the SW radiation reaching the surface: calculations using the parameterisations of
315 *Lacis and Hansen* (1974) indicate a maximum difference at local noon of around 16Wm^{-2}. This
316 change in down-welling SW irradiance due to changes in column water vapour loading is accounted
317 for in our calculations.
318
319 Figure 10a shows the ratio of the diffuse to the direct fluxes between 14:00 to 18:00 for 18 March
320 2009 (contrail and cloud free) and 20 March 2009 (contrail affected but otherwise cloud free). The
321 effect of contrails can clearly be seen on 20 March 2009 with a significant increase in the
322 diffuse/total radiation at the surface. The more variable nature of the diffuse/total radiation caused by
323 the varying contrail/cirrus optical depth and viewing geometries can also be seen in the data from the
324 20 March when compared to the 18 March.
325
326 Figure 10b shows $\Delta F_{SW\ obs}$ and $\Delta F_{SW\ obs\ \&\ model}$ determined from the two methods described above
327 which show reasonable agreement. The peak ΔF_{SW} is determined to be stronger than -150Wm^{-2} (the
328 minus sign indicating a reduction in SW radiation at the surface). Subsequently ΔF_{SW} is weaker,
329 ranging from around zero to -50Wm^{-2}. Between 14:00 and 17:00 the mean $\Delta F_{SW\ obs}$ is -44Wm^{-2} and
330 the mean $\Delta F_{SW\ obs\ \&\ model}$ is -47Wm^{-2}. Although the modelling method tends to give a slightly higher
331 mean estimate for ΔF_{SW}, no consistent bias is found (e.g. the period between 15:00 and 16:00), and
332 either method may be thought of as a reasonable approximation. A standard deviation of 14 Wm^{-2} is
333 found for both methods, when considering one minute averages, leading to a standard error of
334 around 1Wm^{-2}. The real error estimate is considerably higher owing to potential systematic
335 uncertainties in the total column water vapour and ozone fields and variations in the aerosol optical
336 depth and is estimated as ±10Wm^{-2}.
337

6. Determination of the SW and LW radiative forcing of contrails/cirrus at the top of the atmosphere.

The radiative forcing is determined at the top of the atmosphere by using a methodology similar to that used in *Haywood et al.* (2005). *Haywood et al.* (2005) compared the LW top of the atmosphere clear-sky irradiances derived from the Meteosat-7 instrument with those predicted by the Met Office global NWP model. Differences in the irradiances of up to 50 Wm^{-2} were clearly identified over the Sahara. This feature was shown to be due the omission of the radiative effects of mineral dust in the NWP model. Here we perform a similar exercise; because the NWP model does not accurately represent the ice super-saturation observed between approximately 25,000ft-35,000ft (7.5 to 10.5km) (Figure 3b), no cirrus cloud is modelled in these regions. Just as the study of *Haywood et al.* (2005) does not rely on explicit modelling of the radiative effects of mineral dust, the simulations that we perform here do not rely on explicit modelling of the radiative effects of contrail-induced cirrus. The estimates presented here are therefore independent of the retrievals derived in section 4.

6.1. Definition and diagnosis of the radiative forcing

The radiative forcing at the top of the atmosphere, ΔF_{SW_TOA}, of the contrail induced cirrus can be simply diagnosed as:-

$$\Delta F_{SW\_TOA} = SW_{\uparrow \text{no contrails}} - SW_{\uparrow \text{contrails}} \quad (3)$$

or

$$\Delta F_{SW\_TOA} = SW_{\uparrow \text{model}} - SW_{\uparrow \text{satellite.}} \quad (4)$$

Similarly the long-wave radiative forcing, ΔF_{LW_TOA}, can be diagnosed from:-

$$\Delta F_{LW\_TOA} = LW_{\uparrow \text{no contrails}} - LW_{\uparrow \text{contrails}} \quad (5)$$

or

$$\Delta F_{LW\_TOA} = LW_{\uparrow \text{model}} - LW_{\uparrow \text{satellite.}} \quad (6)$$

364 Previous studies have derived top of the atmosphere irradiances from radiance data from either the
365 Meteosat-7 instruments (*Haywood et al.*, 2005) or the Geostationary Earth Radiation Budget
366 (GERB) instrument (*Allan et al.*, 2007). In this study we diagnose $SW_{\uparrow satellite}$ and $LW_{\uparrow satellite}$ from the
367 SEVIRI instrument. Broadband irradiance is routinely estimated from narrow-band channels of the
368 SEVIRI instrument by the Royal Meteorological Institute of Belgium in the processing of GERB
369 data. Processing is conducted on 3x3 SEVIRI pixels at an approximate pixel resolution over the UK
370 of 15km. Conversion of narrow to broad-band radiances is achieved using a regression technique
371 combined with detailed calculations from line-by-line radiative transfer simulations (*Clerbaux et al.*
372 2008a) and are converted to irradiance using a set of angular distribution models; this is essentially
373 the same method as described in *Haywood et al.* (2005) for Meteosat-7 but exploiting the greater
374 number of channels supplied by SEVIRI. For the shortwave region of the spectrum, a similar
375 approach is adopted, using 3 shortwave channels from SEVIRI in the regression and applying
376 angular dependence models from the Clouds and the Earth's Radiance Energy System (CERES)
377 dataset to estimate broadband shortwave irradiance (*Clerbaux et al.* 2008b).
378
379 Since GERB data was only produced between 02:00 and 07:00 during the period of interest, we use
380 the SEVIRI-based estimates of $SW_{\uparrow satellite}$ and $LW_{\uparrow satellite}$. To reduce the effect of slight timing
381 differences between the model and the SEVIRI data, $SW_{\uparrow satellite}$ is scaled by the ratio of the incoming
382 shortwave radiation for the model and the satellite data
383
384 Interpolating SEVIRI $LW_{\uparrow satellite}$ to the GERB grid, comparisons were conducted over 140 grid
385 points over the UK region for 03:00 and 06:00 on the 20 and 21 March 2009. A mean bias of 0.7
386 Wm^{-2} and root mean squared difference of 3.2 Wm^{-2} between SEVIRI and GERB estimates are
387 apparent. Based on the expected SEVIRI calibration and the processing described in *Clerbaux et al.*
388 (2008a,b) we propose a conservative estimate of uncertainty of order 5%, which corresponds to
389 ± 12.5 Wm^{-2} for an irradiance of 250 Wm^{-2}: a similar uncertainty is assumed for $SW_{\uparrow satellite}$.

To diagnose $SW_{\uparrow model}$ and $LW_{\uparrow model}$ we use the TOA fluxes from the high resolution operational UK4 model (*Lean et al.*, 2008) which have a spatial resolution of 4km in the horizontal and contains 70 model levels. The model is initialised at 00:00 and is run forward with no data assimilation for a period of 36hours. Data assimilation is turned off to prevent the model from moistening the upper troposphere via assimilation of observational data sets and hence we deliberately inhibit any cirrus cloud formation. The model time-step is 100seconds with radiation being called every 9 timesteps (15 minutes). The model contains a basic aerosol climatology (*Cusack et al.*, 1998). The SW surface reflectance is determined from the combined reflectance of 9 representative surface types as described in the Met Office Surface Exchange Scheme II (MOSES II, *Essery et al.*, 2003) and the surface emissivity is uniformly set to a spectrally independent value of 0.97. The radiation scheme in the model is the *Edwards and Slingo* (1996) radiation code which is configured to treat the absorption and scattering of SW and LW radiation by gases, aerosols, and water and ice clouds. The radiation code contains 5 bands in each of the SW and LW regions of the spectrum and the 2-stream approximation is used. Note here that the irradiances derived from the UK4 model are very similar to those from the global model: we chose to present the analysis of the UK4 model only as this model has superior spatial resolution.

6.2. Approach to cloud screening

The cloud screening approach that is used here differs when applied to satellite and the model data.

Low lying stratocumulus clouds have less impact on LW radiation than SW radiation at the top of the atmosphere because the difference in the temperature between the top of the low level liquid water clouds is only a few degrees different from the surface of the ocean whereas the change in the SW reflectivity change can be significant. Consider the tephigrams in Figure 3, particularly the Ekofisk ascent in the North Sea. Although no stratocumulus cloud was present at this location, the

relative humidity was 88% at 993hPa. The difference between the temperature at 993hPa and 1026hPa (the highest recorded pressure approximately corresponding to 29m altitude) was less than 4K. Calculations show that differences of 4-6K at temperatures of around 280K correspond to flux differences of around 6-9% or 13-20Wm^{-2} for TOA fluxes of 220Wm^{-2}. Thus, in terms of TOA LW irradiances, areas where stratocumulus cloud is forecast in the model but not present in the observations (or vice versa) will lead to an error estimated as approximately ±20Wm^{-2}. We therefore assign an error estimate of ±20Wm^{-2} over areas where cloud is present in either the model or the satellite retrievals.

For $SW_{\uparrow satellite}$ over oceans, areas where the cloud retrievals described in section 4 reveal the influence of low level water cloud are screened out of the analyses. Over land, for optically thin clouds, the retrievals fail (section 4) and liquid water cloud is diagnosed. This problem is overcome by applying a threshold that removes all areas of liquid cloud with optical thickness at 0.55μm greater than 2. For $SW_{\uparrow model}$, areas with significant liquid water cloud are screened out from the data. While it is recognised that these masking thresholds have some degree of subjectivity associated with them, the results presented in 6.3 appear entirely reasonable.

6.3. Results

The resulting $LW_{\uparrow satellite}$, $LW_{\uparrow model}$, and ΔF_{LW_TOA} with no cloud screening applied are shown for 14:00 in Figure 11a, b, and c respectively. Figure 11a shows $LW_{\uparrow satellite}$ of greater than 260Wm^{-2} over land areas of the UK and the continent. Lower values of around 250Wm^{-2} are evident in clear skies over the ocean owing to the lower surface temperature. The lowest values of all are apparent over the North Sea and over eastern areas of England where a $LW_{\uparrow satellite}$ of less than 220Wm^{-2} is evident; these areas correspond to the presence of either thick low level stratocumulus clouds, or thin high level contrail-induced cirrus. Figure 11b indicates that $LW_{\uparrow model}$ shows many similar features to $LW_{\uparrow satellite}$: the highest values over land regions, lower values over clear-sky ocean regions, and the

lowest values over thick modelled stratocumulus regions are all present. The feature that is clearly absent is the low values (< 220-230 Wm^{-2}) associated with the optically thin contrail-induced cirrus cloud. ΔF_{LW_TOA} obtained from equation (6) shows strong positive values which exceed $+40Wm^{-2}$ in the vicinity of the CCC (see area labelled (i) on Fig 11c). The strong spatial correlation between ΔF_{LW_TOA} and the polar orbiting satellite image of the CCC shown in Figure 5e and the modelled position of the CCC shown in Figure 6e is clearly evident. A second area where ΔF_{LW_TOA} exceeds $+40Wm^{-2}$ is also shown in Figure 11c (labelled (ii)) which appears to correspond to contrails initiated off the east coast of Scotland (see Figure 5). There are several areas where ΔF_{LW_TOA} is diagnosed as being negative – areas of SW England, Wales, northern Scotland and the continent all exhibit ΔF_{LW_TOA} as strong as $-15Wm^{-2}$. Interestingly, no significant biases are evident over clear sky ocean areas. The biases over land areas are likely related to a cold bias in the surface temperature in the UK4 model (*J.M. Edwards, personal communication*) which is currently under investigation, but beyond the scope of the present work.

The resulting $SW_{\uparrow satellite}$, $SW_{\uparrow model}$, and ΔF_{SW_TOA} with no cloud screening applied are shown for 14:00 in Figure 11d, e, and f respectively. It is immediately apparent that the differences between the modelled and measured irradiances over the stratocumulus clouds in the North Sea are far larger in the SW region of the spectrum than in the LW region, with SEVIRI generally diagnosing brighter clouds by in excess of $150Wm^{-2}$ in many areas. The liquid water cloud mask for SEVIRI (sections 4 and 6.2) are encompassed by the thick contour intervals on Figure 11d surrounding the extensive stratocumulus in the North Sea and another less extensive area of stratocumulus over SW Scotland. Liquid water cloud present in the model is encompassed by the thick contour line shown in Figure 11e. Generally, the model does a reasonable job of predicting the presence and areal extent of the stratocumulus regions in both the North Sea and SW Scotland. There are areas where the model contains cloud where the SEVIRI retrieval does not or vice-versa. For example the model extends the stratocumulus sheet in the North Sea further south than the SEVIRI retrieval and SEVIRI shows

more extensive stratocumulus to the extreme north west of the images shown. The composite cloud mask determined in Figure 11f contains all areas where liquid water cloud is diagnosed in either the SEVIRI retrieval or the model and is indicated once more by areas falling within the thick contour line. This composite cloud screening algorithm is used henceforth in screening data for liquid water cloud via a simple cloud mask.

ΔF_{LW_TOA} and ΔF_{SW_TOA} including the cloud mask are shown in Figure 12 for the period 12:00 to 18:00. No ΔF_{SW_TOA} is shown for 18:00 because the sun had set. The areas of maximum ΔF_{LW_TOA} and ΔF_{SW_TOA} associated with the contrail-induced cirrus are shown to drift southwards in agreement with the observations in Figure 5 and the modelling in Figure 6. ΔF_{LW_TOA} has values stronger than $45 Wm^{-2}$ throughout the period (Figure 12a-d). On the other hand, ΔF_{SW_TOA} shows values stronger than $-75 Wm^{-2}$ in the predicted position of the CCC at 14:00 (Figure 12f). As a consequence, there is significant cancellation of ΔF_{LW_TOA} and ΔF_{SW_TOA} as is clearly shown in ΔF_{net_TOA} (Figure 12h-j). The temporal evolution of the mean ΔF_{LW_TOA}, ΔF_{SW_TOA} and ΔF_{net_TOA} over the domain encompassed by the thick contour on Figure 12 are shown in Figure 13a.

Figure 13a shows that, during daylight hours ΔF_{LW_TOA} is significantly offset by ΔF_{SW_TOA} leading to a ΔF_{net_TOA} of around $+10 Wm^{-2}$ during the period 11:00 – 15:00. ΔF_{net_TOA} becomes negative when the solar zenith angle increases towards sunset owing to the stronger contribution from the SW component as expected from detailed radiative modelling of the SW and LW radiative effects (*Myhre and Stordal*, 2001). At sunset ΔF_{net_TOA} is simply equal to ΔF_{LW_TOA}. Note that ΔF_{SW_TOA} becomes more negative during afternoon until immediately before sunset, at a rate that is faster than the ΔF_{LW_TOA} becomes more positive. This is consistent with the increase in SW forcing, due to the dependence of the contrail albedo on solar zenith angle, as was discussed in, for example, Myhre and Stordal (2001).

494 The areal extent of the contrail-induced cirrus is defined as areas where ΔF_{LW_TOA} is greater than
495 twice the standard deviation of ΔF_{LW_TOA} in the domain shown in Figure 12 for each time-frame.
496 Alternative thresholds based on the standard deviation or even a single threshold could be applied,
497 but our method has the advantage of factoring in the temporal variability of ΔF_{LW_TOA}. Figure 13b
498 shows the area extent of the contrail induced cirrus is shown to steadily increase from around
499 28,000km^2 at 11:00 to 52,000km^2 by 17:00 after which it decays. Note that no areas outside the
500 domain shown are classified as contrail-induced cirrus throughout the sequence shown indicating
501 that the cirrus has not simply advected out of the domain. Thus, the area of the contrail induced
502 cirrus approximately doubles in size over a 6 hour period. We also calculate the areal extent of the
503 CCC from the NAME model results: these are also shown on Figure 13b. The CCC covers
504 approximately 9,000km^2 at 11:00, growing to approximately 34,000km^2 by 20:00 and is on average
505 23,000km^2. The rate of increase in the contrail area is similar between the contrail-induced cirrus
506 derived over the entire domain and that derived for the CCC until around 17:00. After 17:00 the
507 CCC continues to grow while the area contrail-induced cirrus over the domain starts to diminish.
508 This indicates that conditions for continued contrail-induced cirrus growth cease around this time.
509 The reasons for this transition from conditions of contrail-induced cirrus growth to conditions of
510 contrail-induced cirrus decay are beyond the scope of this study.
511
512 ΔF_{LW_TOA}, and ΔF_{SW_TOA} may also be calculated for the Cardington site. Because the scattering of
513 visible radiation by contrail-induced cirrus should be essentially conservative, ΔF_{SW_TOA} should be
514 roughly comparable to ΔF_{SW} determined at the surface (see section 5, and Figure 9). This
515 comparison will be affected by the amount of absorption of near-IR by water vapour in the column
516 between the CCC and the surface. ΔF_{SW_TOA} is evaluated from the 7 grid-boxes closest to
517 Cardington, for 12:00 and at each hour through to sunset at around 18:00; the mean value for
518 ΔF_{SW_TOA} over the period 14:00-17:00 is -36.5Wm^{-2}, which is in reasonable agreement with the
519 surface ΔF_{SW} of between -44.4Wm^{-2} to -47.3Wm^{-2} ± 10Wm^{-2} determined from the in-situ

measurements. As in the calculations over the entire domain (Figure 12), ΔF_{LW_TOA} for the same period for the Cardington site reveals an almost complete cancellation of the SW and LW effects with ΔF_{LW_TOA} being computed as $+35.3 Wm^{-2}$.

7. Discussion and conclusions.

The formation of persistent contrails and their evolution into contrail-induced cirrus clouds are illustrated. While it is not possible to be 100% certain that cirrus clouds would not have formed in the absence of aviation activity, the balance of evidence, which includes the spatial coherence of the contrail induced cirrus and modelling its position, very strongly suggests that the cirrus cloud is of aviation origin.

The persistence of the contrails and contrail-induced cirrus is remarkable. The persistent contrail formed at ~08:30 on the 20 March 2009 (Figure 5 and Figure 6) is still clearly evident as contrail-induced cirrus some 12 hours after formation. In fact, as noted in section 4, contrail-induced cirrus initiated during daylight hours of the 20 March are clearly present in satellite imagery at 03:32 on 21 March 2009.

Our study confirms the fact ΔF_{net_TOA} from contrail induced cirrus is the relatively small residual derived from strong ΔF_{LW_TOA} and ΔF_{SW_TOA} components of opposite signs which has been known for some time (e.g. *Fahey et al.*, 1999 *and references therein, Stuber et al.,* 2006). However, to our knowledge, this is the first time that this has been proved without relying on explicit modelling of contrail induced cirrus microphysics. While the results from this study have to be considered to be a specific case study, it does question the merits of rescheduling aircraft flights from night to day flights which have been suggested to make maximum benefit of the negative radiative forcing owing to the reflection of solar radiation (e.g. *Myhre and Stordal*, 2001, *Stuber et al*., 2006). If contrails spread into contrail-induced cirrus and the cirrus has a lifetime of some 18 hours as in this study,

546 then initiating the contrail between 00:00 and 06:00 on the 20 March 2009 would maximise the
547 exposure of the contrail-induced cirrus to solar radiation. Of course, this calculation must be
548 considered very speculative given our current understanding of the complexities of contrail-induced
549 cirrus.
550
551 It is interesting to ask to what degree the radiative forcing from aviation is enhanced owing to the
552 formation of the contrail-induced cirrus in this episode: here we make a simple estimate by
553 considering solely the influence of the CCC that we presume is formed by the AWACS aircraft. We
554 chose to compare our estimate of the radiative forcing against that from persistent contrails from the
555 entire aviation fleet, as to compare against the radiative forcing from other emissions such as carbon
556 dioxide would be misleading because of the disparate residence times of contrail-induced cirrus and
557 carbon dioxide. The approximate area influenced by the CCC (Figure 6 and Figure 13) is estimated
558 to be 23,000km^2, and the radiative forcing ΔF_{net_TOA} is assumed to be +10Wm^{-2} during daylight
559 hours and +30Wm^{-2} during night-time hours (Figure 13), acting from approximately 09:00 until
560 03:00 the next day. We assume that sunlight hours extend from 06:00 until 18:00, then the SW and
561 LW effects act together for the first 9 hours and LW effects act alone for the remaining 9 hours, so
562 that the *local* mean forcing is about 20 Wm^{-2} for an 18 hour period or 15Wm^{-2} for a 24 hour period.
563 This is equivalent to a *global* mean radiative forcing in the 24hour period of ~0.7mWm^{-2}. Hence,
564 this *single* event may have caused a forcing which is an appreciable fraction (7%) of the diurnally
565 averaged global-mean persistent contrail forcing (10 mWm^{-2}). Alternatively, when averaged over a
566 year, the event generated by the AWACS aircraft contributes approximately 2μWm^{-2} or 0.02% of the
567 annual global mean radiative forcing from persistent contrails from the entire fleet of civil aircraft:
568 5000 such events/year would need to occur to generate a global annual mean radiative forcing of 10
569 mWm^{-2}.
570

We can also estimate the distance flown by the AWACS aircraft (10 complete circles of 40km diameter ~ 1250km) and the distance flown by the entire civil aviation fleet (3.3×10^{10}km, on an annual basis, *Eyres et al*, 2004). If we consider the best estimate for the global mean radiative forcing due to persistent contrails to be $10 mWm^{-2}$ then the entire civil fleet contributes a radiative forcing/km due to persistent contrail formation of around $3 \times 10^{-13} Wm^{-2}$/km. The AWACS aircraft exerts a global annual mean forcing of approximately $2 \mu Wm^{-2}$ for a distance travelled of 1250km leading to a radiative forcing/km due to contrail-induced cirrus of $1.6 \times 10^{-9} Wm^{-2}$/km: this is over 5000 times greater indicating that aviation operations that generate contrail-induced cirrus exert a disproportionately high radiative forcing and hence warming of the climate system.

Of course, it is possible that natural cirrus could have been generated in the absence of the AWACS and other aircraft operations. The very high supersaturation with respect to ice in this specific case study mean that other meteorological 'triggers' causing the downstream evolution of natural cirrus cannot be ruled out. To establish that natural cirrus would not have formed in the absence of the aircraft operations would require very accurate modelling of processes that are only crudely represented in current numerical weather prediction models.

These calculations emphasize the importance of obtaining a reliable estimate of the global role of contrail-induced cirrus, and understanding the extent to which they add to natural cirrus cover. In this particular instance, because of the distinct pattern of the original contrails, it has been possible to follow, with some degree of confidence, the causal sequence from contrails to contrail-induced cirrus. In normal circumstances this would not be possible and it will be important to ascertain whether the sequence of events, and the size of the effect, that we have inferred is a regular occurrence.

This work indicates that a confident assessment of the total effect of aviation on climate, and the efficacy of possible mitigation options (for example, changing flight routing or altitudes to avoid contrail formation, with the possibility that, for example, CO_2 emissions will increase as a result) is heavily dependent on reducing the uncertainty in the size of the contrail-induced radiative forcing.

Acknowledgements: The authors would like to thank James MacGregor for providing the data from the Cardington Field Site and Richard Forbes for providing the ECMWF model output. Colleagues at the Chilbolton observatory are thanked for providing lidar data. RA was funded by a NERC Advanced Fellowship NE/C51785X/1 and the National Centre for Earth Observation. GR and AR are supported by the NERC COSIC project. Gunnar Myhre is thanked for very useful comments on an earlier version of the manuscript.

References

Allan, R. P., A. Slingo, S.F. Milton and M.A. Brooks, 2007, Evaluation of the Met Office global forecast model using Geostationary Earth Radiation Budget (GERB) data, *Q. J. Roy. Meteorol. Soc.*, 133, 1993-2010.

Clerbaux, N., S. Dewitte, C. Bertrand, D. Caprion, B. De Paepe, L. Gonzalez, A. Ipe, and J.E. Russell, 2008a: Unfiltering of the Geostationary Earth Radiation Budget (GERB) Data. Part II: Longwave Radiation. J. Atmos. Oceanic Technol., 25, 1106-1117.

Clerbaux, N., S. Dewitte, C. Bertrand, D. Caprion, B. De Paepe, L. Gonzalez, A. Ipe, J.E. Russell, and H. Brindley, 2008b: Unfiltering of the Geostationary Earth Radiation Budget (GERB) Data. Part I: Shortwave Radiation. J. Atmos. Oceanic Technol., 25, 1087-1105.

Cusack, S., A. Slingo, J.M. Edwards, and M. Wild, 1998; The radiative impact of a simple aerosol climatology on the Hadley Centre GCM. *Q. J. R. Meteor. Soc*. 124: 2517-2526.

Edwards, J. M., and A. Slingo (1996), Studies with a flexible new radiation code: I. Choosing a configuration for a large scale model, *Q. J. R. Meteorol. Soc*., 122, 689– 720.

Essery, R. L. H., M. J. Best, R. A. Betts, P. M. Cox, and C. M. Taylor (2003), Explicit representation of subgrid heterogeneity in a GCM land surface scheme, *J. Hydrometeorol.*, 4, 530– 543.

Eyers, C., P. Norman, J. Middel, M. Plohr, S. Michot, K. Atkinson, and R. Christou, 2004: AERO2k global aviation emissions inventories for 2002 and 2025. Technical report, QinetiQ Ltd., Farnborough, UK, qinetiq/04/01113.

Fahey, D., U. Schumann, S. Ackerman, P. Artaxo, O. Boucher, M.Y. Danilin, B. Kärcher, P. Minnis, T. Nakajima, and O.B. Toon, 1999.Aviation-produced aerosols and cloudiness. *Aviation and the Global Atmosphere*. Intergovernmental Panel on Climate Change. J.E. Penner, D.H. Lister, D.J. Griggs, D.J. Dokken, and M. McFarland (eds), Cambridge University Press, Cambridge, United Kingdom and New York, NY, USA, 65-120.

Forster, P., et al., 2007: Changes in Atmospheric Constituents and in Radiative Forcing. In: Climate Change 2007: The Physical Science Basis. Contribution of Working Group I to the Fourth Assessment Report of the Intergovernmental Panel on Climate Change [Solomon, S., D. Qin, M. Manning, Z. Chen, M. Marquis, K. B. Averyt, M. Tignor and H. L. Miller (eds.)]. Cambridge University Press, Cambridge, United Kingdom and New York, NY, USA.

Haywood, J.M, Allan, R.P., Culverwell I., Slingo, A., Milton, S., Edwards. J.M., and Clerbaux, N., Can desert dust explain the outgoing longwave radiation anomaly over the Sahara during July 2003? *J. Geophys. Res*., 110, D05105, doi:10.1029/2004JD005232, 2005.

IPCC Special Report on Aviation and the Global Atmosphere, J. E. Penner, D. H. Lister, D. J. Griggs, D. J. Dokken, and M. McFarland (Eds.), *Cambridge University Press*, Cambridge, UK, 1999.

IPCC (2007) WGI. Climate Change 2007: The Physical Science Basis. Contribution of Working Group I to the Fourth Assessment Report of the Intergovernmental Panel on Climate Change [Solomon, S., D. Qin, M. Manning, Z. Chen, M. Marquis, K. B. Averyt, M. Tignor and H. L. Miller (eds.)]. *Cambridge University Press*, Cambridge, United Kingdom and New York, NY, USA.

Jones AR. 2004. Atmospheric dispersion modelling at the Met Office. Weather 59: 311–316.

Kärcher, B., and P. Spichtinger, Cloud-controlling factors of cirrus. Heintzenberg, J., and R. J. Charlson, eds. Clouds in the Perturbed Climate System: Their Relationship to Energy Balance, Atmospheric Dynamics, and Precipitation. Strüngmann Forum Report, vol. 2. Cambridge, MA: MIT Press ISBN 978-0-262-01287-4 pp 235-267.

Lacis, A.A., and Hansen, J.E., 1974, A parameterization for the absorption of solar radiation in the Earth's atmosphere, *J. Atmos. Sci*., 31, 118-131.

Lean, H.W., P.A. Clark, M. Dixon, N.M. Roberts, A. Fitch, R. Forbes, and C, Halliwell, Characteristics of High-Resolution Versions of the Met Office Unified Model for Forecasting Convection over the United Kingdom, Monthly Weather Review, 136, 9, 3408-3424, 2008

Lee, D.S., D.W.Fahey, P. M.Forster, P.J.Newton, L.L.Lim, B.Owen and R.Sausen. Aviation and global climate change in the 21st century, Atmospheric Environment (to appear) 2009.

Mannstein, H. and U. Schumann, Aircraft induced contrail cirrus over Europe, Meteorologische Zeitschrift, Vol. 14, No. 4, 549-554. 2005

Mannstein, H. and U. Schumann, Corrigendum to Mannstein, H. and U. Schumann, 2005 Aircraft induced contrail cirrus over Europe, Meteorologische Zeitschrift, Vol. 14, No. 4, 549-554. Meteorologische Zeitschrift, 16, 131-132, 2007

Minnis, P., D.F. Young, D.P. Garber, L. Nguyen, W.L. Smith, and R. Palikonda, Transformation of contrails into cirrus during SUCCESS, *Geophys. Res. Letts*, 25, 8, 1157-1160, 1998.

Minnis, P., Kirk Ayers, J., Palikonda, R., and Phan, D.: Contrails, Cirrus Trends, and Climate, J. Climate, 17, 1671–1685, 2004.

Myhre, G. and Stordal, F. On the tradeoff of the solar and thermal infrared radiative impact of contrails. *Geophys. Res. Lett.* 28, 3119–-3122 (2001).

Nakajima, T., and King, M. D. (1990): Determination of the optical thickness and effective particle radius of clouds from reflected solar radiation measurements. Part I: Theory. *Journal of the Atmospheric Sciences*, 47, 1878-1893.

Newman, S.M., Hilton, F., Collard, A. 2008. Identification of biases in the modelling of high peaking water vapour channels from IASI. *Tech Proc 16th Int TOVS Study Conference*, Angra dos Reis, Brazil, 6-13 May 2008.

Prather, M., Sausen, R., Grossman, A.S., Haywood, J.M., Rind, D., Subbaraya, B.H., 1999. Potential climate change from aviation. Aviation and the Global Atmosphere. Intergovernmental Panel on Climate Change. J.E. Penner, D.H. Lister, D.J. Griggs, D.J. Dokken, and M. McFarland (eds), Cambridge University Press, Cambridge, United Kingdom and New York, NY, USA, 185-215, 373pp.

Rädel G, Shine KP 2007: Evaluation of the use of radiosonde humidity data to predict the occurrence of persistent contrails. *Quart J Roy Meteorol Soc* 133: 1413–1423 DOI: 10.1002/qj.128

Rädel G, Shine KP 2008: Influence of aircraft cruise altitudes on radiative forcing by persistent contrails. *J Geophys Res* 113, D07105 doi:10.1029/2007JD009117.

Rap, A., P.M. Forster, A. Jones, O. Boucher, J.M. Haywood, and R.R. De Leon, Parameterisation of contrails in the UK Met OfficeClimate Model, *submitted to J. Geophys. Res*., 2009.

Rodgers, C.D., 1967. The radiative heat budget of the troposphere and lower stratosphere, Report No A2, Planetary Circulations Project, Dept of meteorology, MIT.

Ryall DB, Maryon RH. 1998. Validation of the UK Met Office's NAME model against the ETEX dataset. *Atmos. Environ.* 32: 4265–4276.

Sausen, R., I. Isaksen, V. Grewe,D. Hauglustaine, D.S. Lee, G. Myhre, M.O. Köhler, G. Pitari, U. Schumann, F. Stordal, and C. Zerefos, 2005, Aviation radiative forcing in 2000: An update on IPCC (1999), *Meteorologische Zeitschrift*, **14**, 555-561.

Stordal, F. G. Myhre, E. J. G. Stordal, W. B. Rossow, D. S. Lee, D.W. Arlander, and T. Svendby, 2005, Is there a trend in cirrus cloud cover due to aircraft traffic? *Atmos. Chem. Phys,* **5**, 2155-2162.

Stuber, N. P. Forster, G Rädel, and K. P.Shine, 2006The importance of the diurnal and annual cycle of air traffic for contrail radiative forcing, Vol 441, doi:10.1038/nature04877, , 864-867.

Vömel, H., H. Selkirk, L. Miloshevich, J. Valverde-Canossa , J. Valdès, E. Kyrö, R. Kivi, W. Stolz, G. Peng and J.A. Diaz, 2007Radiation dry bias of the Vaisala RS92 humidity sensor, *J. Atmos. Ocean. Tech*, , 24, 953.

Figures.

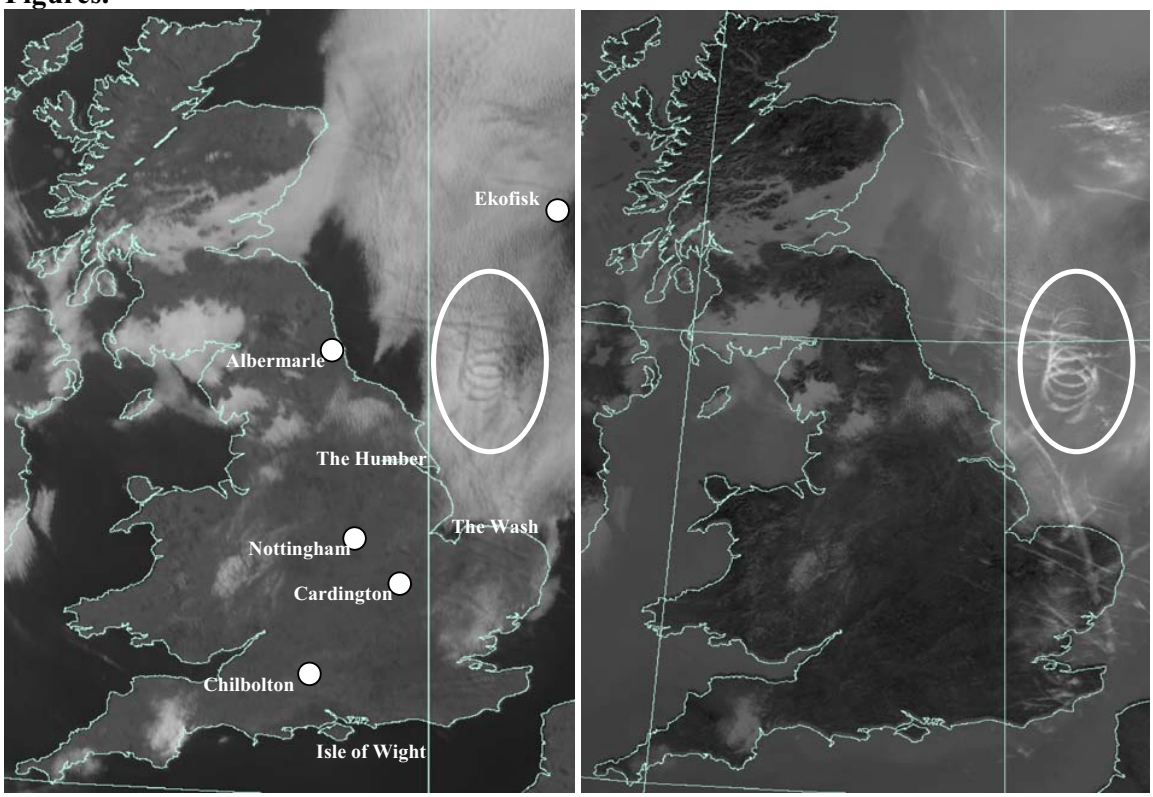

Figure 1. a) high resolution visible image (0.65μm) from the SEVIRI sensor on Meteosat-9 b) infra-red (10.8μm) image obtained from the METOP satellite. Both images are from ~10:40 on 20th March 2009. The white oval highlights the position of the coil-shaped contrail/cirrus (CCC). The positions of the WMO radiosonde ascent sites at Nottingham, Albermarle, and Ekofisk are also shown together with the approximate position of the Met Office Cardington field site, and the Chilbolton observatory.

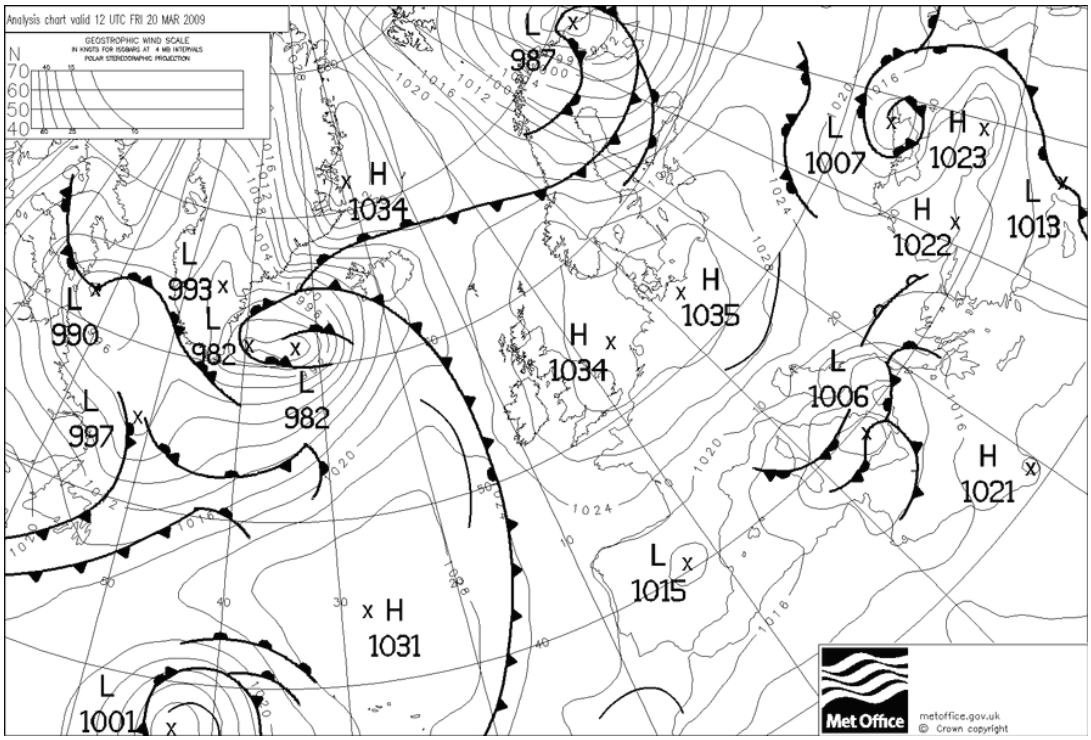

Figure 2. The synoptic surface analysis from the UK Met Office for 12:00 on 20 March 2009.

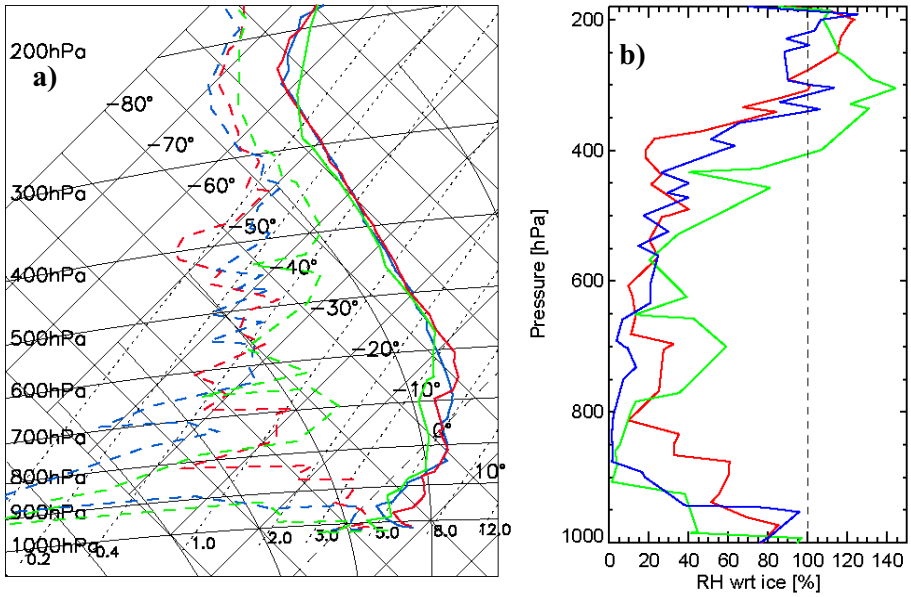

Figure 3. Tephigrams showing a) the radiosonde ascent profiles of temperature and dew point from Nottingham (blue), Albemarle (red), and Ekofisk (green) for 12:00 on March 20th 2009, b) the relative humidity with respect to ice determined from the tephigrams is shown in Figure 2b derived using the correction of *Vömel et al.* (2007).

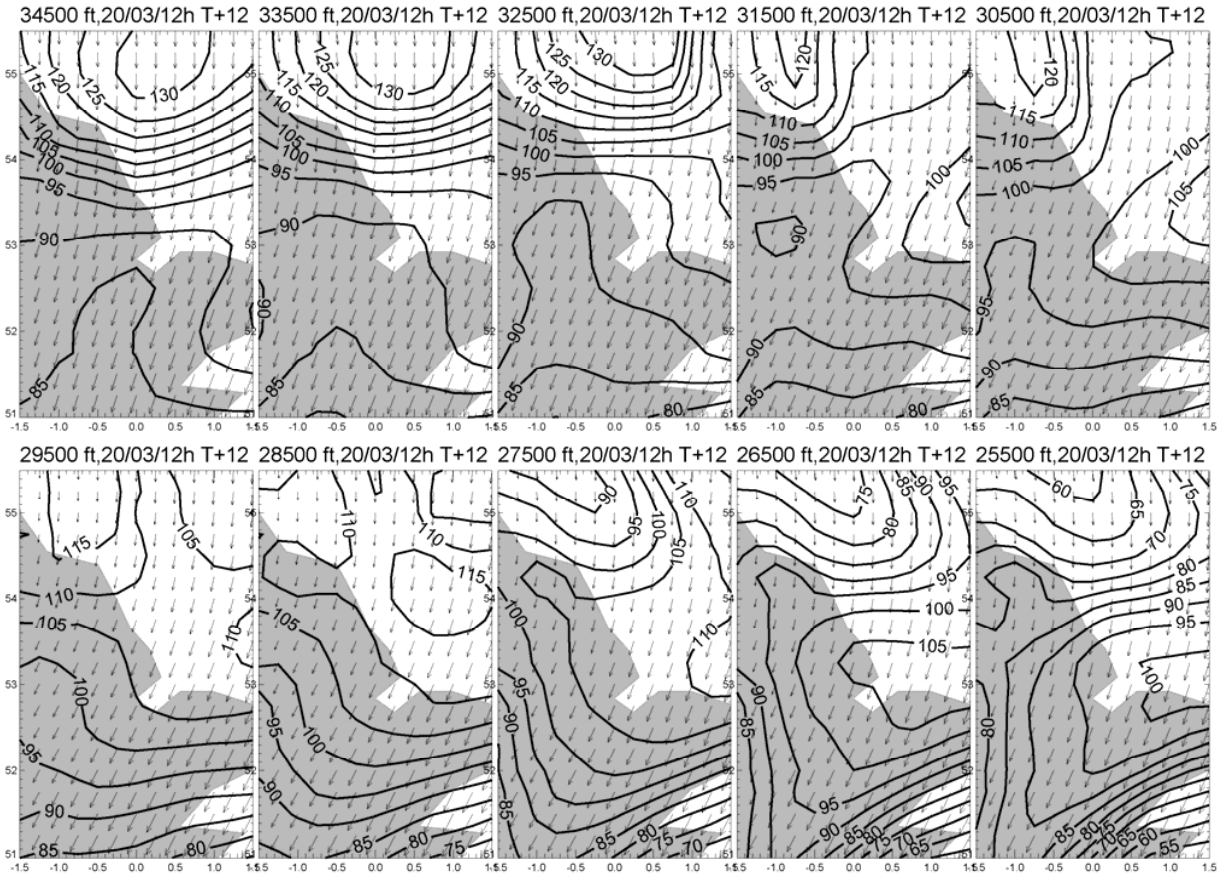

Figure 4. Showing the relative humidity with respect to ice over the UK derived from the ECMWF operational model from 34500ft (top left hand image) to 25500ft (bottom right hand image) and model levels every 1000ft in between. The contours show relative humidity (%), and the arrows represent wind vectors. Fields are for 12:00 on 20 March 2009 from forecasts at 00:00 on 20 March 2009.

Figure 5 IR (10.8μm) images of the formation of contrail induced cirrus (bright white). Areas of stratocumulus are shown as medium grey. The time and satellite is shown in the inset in each of the frames.

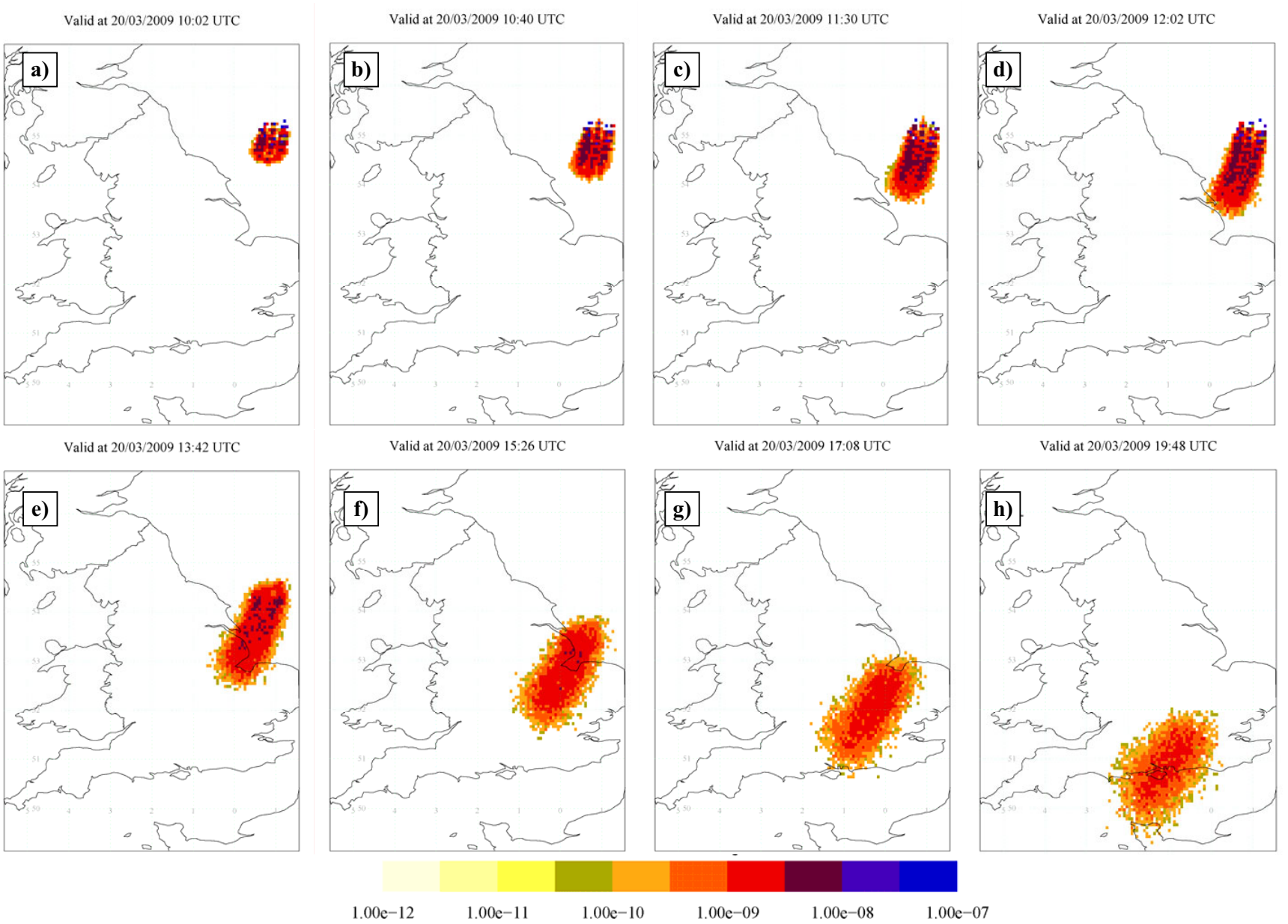

Figure 6. Results from the NAME model initiating a contrail circle at 30,000ft during the period 08:30Z to 11:50Z on 20 March 2009. The units are nominally gm^{-3} from an initial emission of 1g/second.

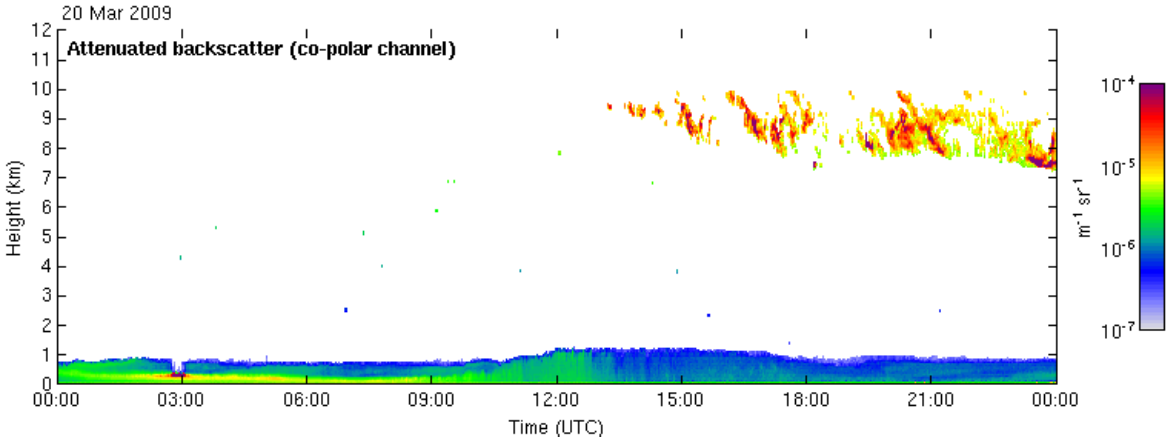

Figure 7. Showing the attenuated back-scatter from the Chilbolton Doppler lidar for 20 March 2009. The main altitude of aviation induced cirrus is seen to be between 8-9km altitude.

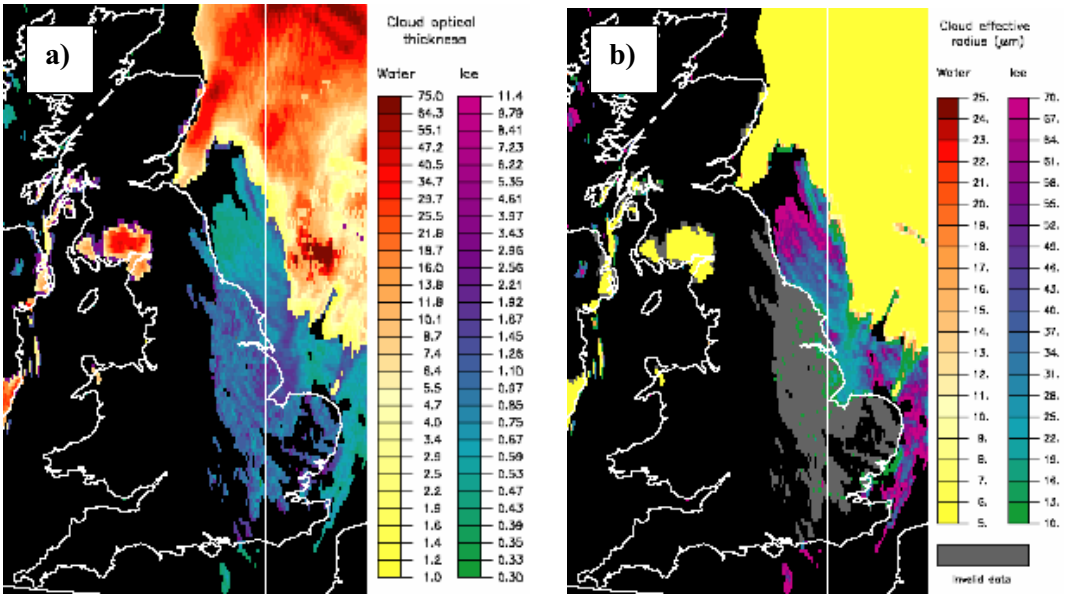

Figure 8. Retrievals of the a) visible (~0.55μm) cloud optical thickness, b) effective radius (μm) for 14:00 on 20 March 2009. The two scales on each plot are for water cloud and for ice cloud respectively.

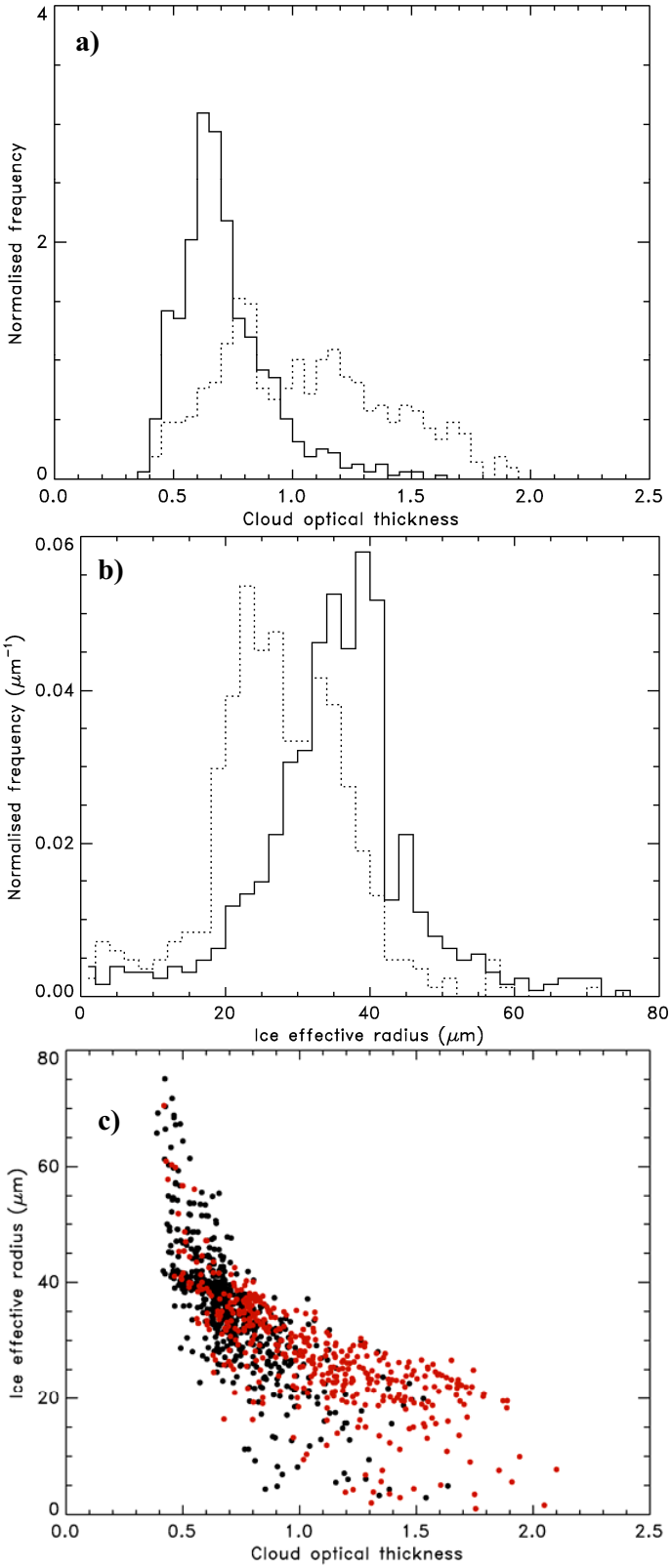

Figure 9. Frequency distributions of a) the cloud optical depth, b) cloud top ice effective radius at 14:00. For each plot, the solid line shows the ice cloud properties derived over the entire domain excluding those from the CCC, while the dotted line shows properties derived for the CCC. c) shows a scatter plot of the ice effective radius against the cloud optical thickness. Black dots indicate points from the entire domain excluding those from the CCC, and red from the CCC.

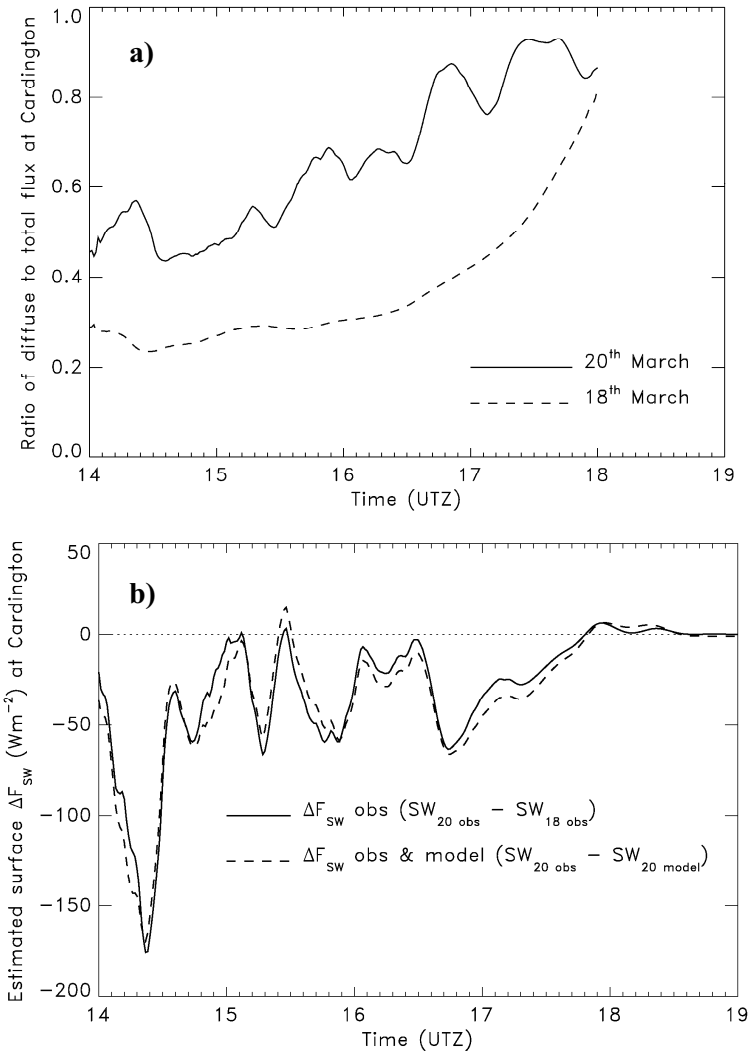

Figure 10. Showing the a) ratio of diffuse to total downward solar irradiance for the 20 March 2009 (contrail case) and for the 18 March 2009 (no contrails), b) the estimated change in the downward surface irradiance (Wm^{-2}) at Cardington derived using two different methods (see text for details).

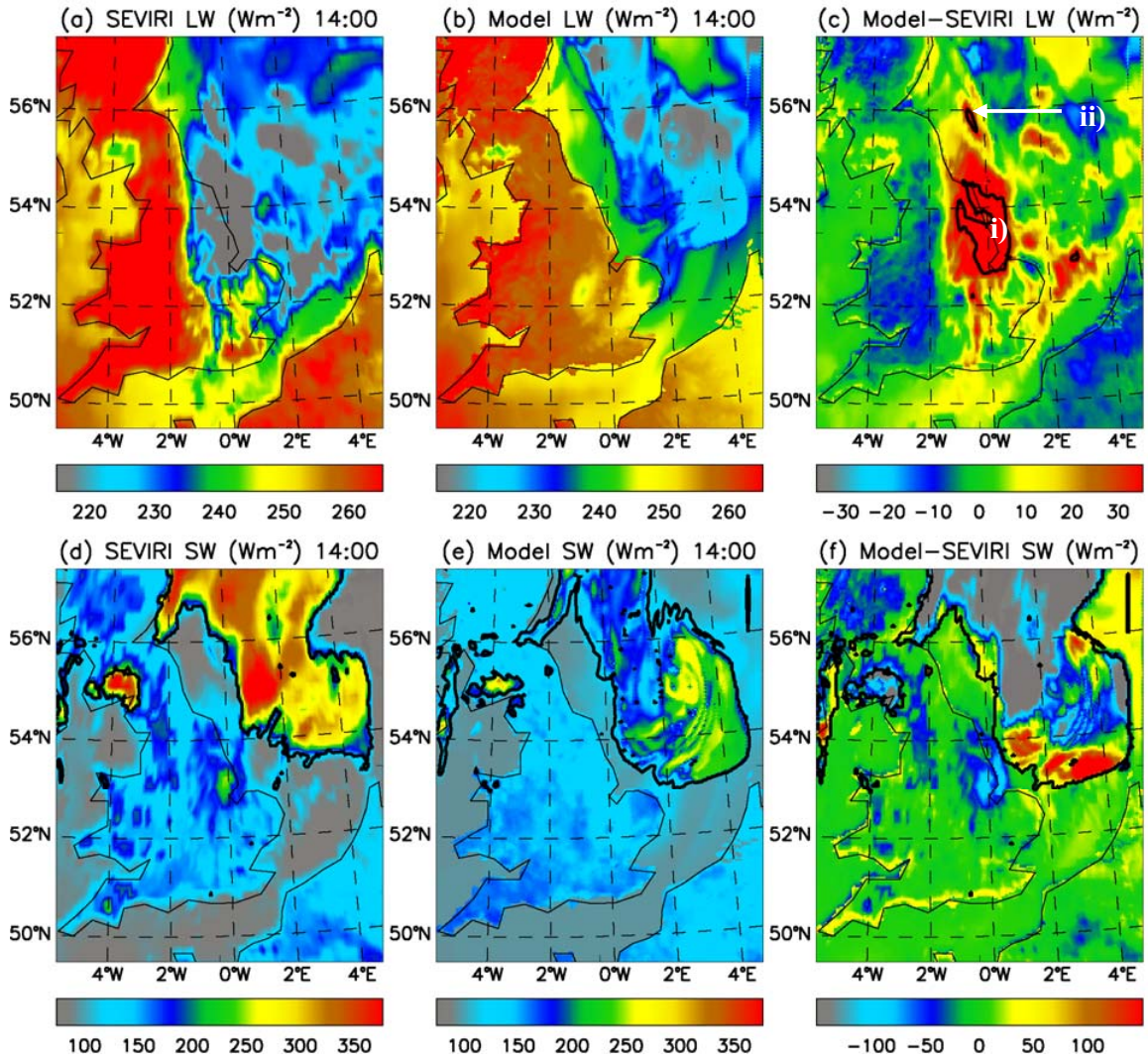

Figure 11. Showing a) $LW_{\uparrow satellite}$, b) $LW_{\uparrow model}$, c) ΔF_{LW_TOA}, d) $SW_{\uparrow satellite}$, e) $SW_{\uparrow model}$, and f) ΔF_{SW_TOA} for the top of the atmosphere for 14:00Z for March 20th, 2009. In c), the contour interval represents $\Delta F_{LW\_TOA} > 40 Wm^{-2}$. In d), e) and f), the contour encompasses areas of liquid water cloud (see text for details of the cloud screening procedure).

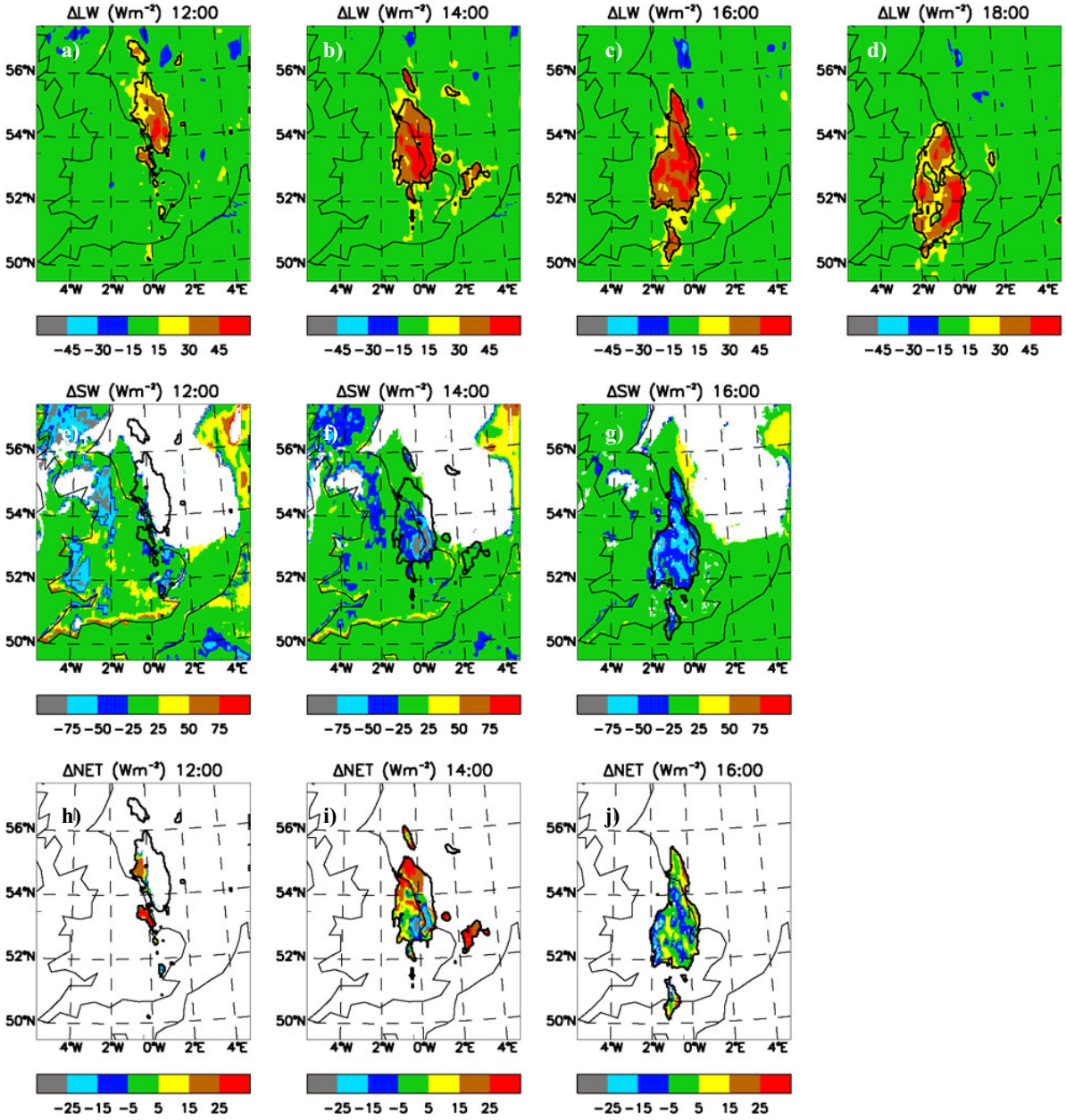

Figure 12. Showing a-d) the evolution of ΔF_{LW_TOA}, e-g) ΔF_{LW_TOA}, and h-j) ΔF_{net_TOA} on the 20 March 2010. The contour interval marked on the figures shows areas defined as contrail as described in the text.

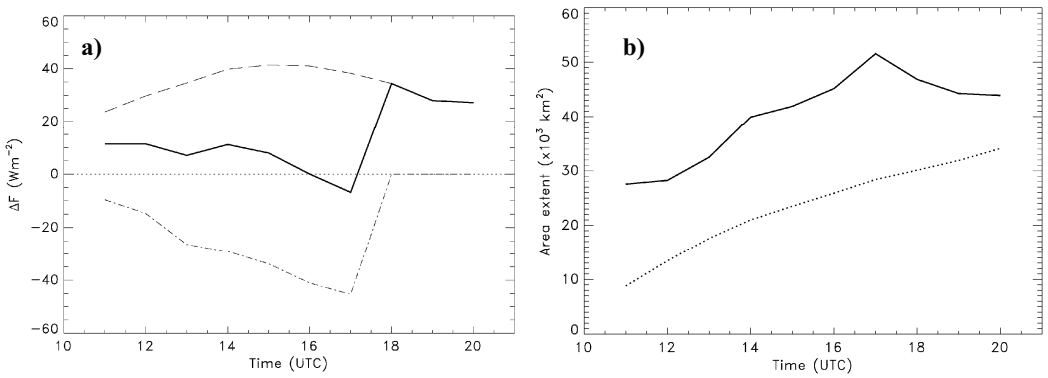

Figure 13. a) ΔF_{LW_TOA}, ΔF_{SW_TOA}, and ΔF_{net_TOA} determined in the area marked by the solid contour on Figure 12 as described in the text. b) The areal extent of the contrail-induced cirrus (in 1000s of km^2) determined from ΔF_{LW_TOA} (solid line) and for the CCC determined from the NAME model (dotted line) as a function of time.